

# Ultrasonic Array Beamforming with Iterative Spatial Filters

Nghia Q. Nguyen<sup>a</sup> and Craig K. Abbey<sup>c</sup> and Michael F. Insana<sup>a,b</sup>

<sup>a</sup>Department of Electrical and Computer Engineering and Beckman Institute

<sup>b</sup>Department of Bioengineering

University of Illinois at Urbana-Champaign, USA

<sup>c</sup>Department of Psychology

University of California at Santa-Barbara, USA

## ABSTRACT

First-principle approaches to the design of medical ultrasonic imaging systems for specific visual tasks are being explored in this paper. Our study focuses on breast cancer diagnosis and is based on the ideal observer concept for visual discrimination tasks, whereby tasks based on five clinical features are expressed mathematically as likelihood functions. Realistic approximations to the ideal strategy for each task are proposed as additional beamforming to maximize diagnostic image information content available to readers. Our previous study showed that a spatial Wiener filter (SWF) beamformer, derived as a stationary approximation of the ideal observer and operating on RF echo data, generally improved discriminability except for one case involving high-contrast lesions. This study explores an adaptive, iterative spatial Wiener filter (ISWF) beamformer that includes a lesion segmentation algorithm to overcome the stationarity assumption and improve discriminability for high-contrast lesions. Predicted performance is compared with that measured from trained human observers using psychophysical methods. We found the greatest feature enhancement of the delay-and-sum beamformer followed by SWF occurs at the image formation step where RF data are converted into B-mode data. The Smith-Wagner computational observer, which operates on the B-mode instead of RF data, was applied to indicate performance lost by envelope detection. ISWF was found to match the performance of SWF for low-contrast lesions and increase the performance for the high-contrast tasks. The ISWF beamforming approach offers greater diagnostic performance for discriminating malignant and benign breast lesions, and it provides a rational basis for further task-specific imaging system design.

**Keywords:** Breast Sonography, ideal observer, image quality, spatial filters

## 1. INTRODUCTION

Medical ultrasonic imaging systems transmit relatively narrow-band (50-100% bandwidth) sound pulses into the body. Echoes produced by interactions with tissue scatterers are measured with an array of phase-sensitive receivers and combined to produce beamformed radio frequency (RF) signals that constitute the lines of a B-mode image. Patient information is encoded in the amplitude and phase of the RF signals, but, because human observers can not process signals with the carrier frequency, RF signal are demodulated before rendering. Such processing of narrow-band, coherently detected echoes that originate from random scattering media generates image speckle.<sup>18</sup> Speckle spots are packets of diagnostic information about tissues, and yet they do not faithfully represent the appearance of organ tissues. Investigators have attempted to reduce the speckled appearance of images by B-mode image processing.<sup>6</sup> The effectiveness of each speckle reduction technique varies depending on the clinical task, but all inevitably reduces diagnostic information.

The *ideal observer* (IO) strategy regarding system design for lesion detection<sup>1,19</sup> suggests that information is maximized by reducing the size and increasing the number of speckle spots. This is achieved by improving the spatial and contrast resolution via enhanced beamforming techniques while maintaining system linearity and

---

Further author information: (Send correspondence to Nghia Q. Nguyen)

Nghia Q. Nguyen: Email: nnguyen6@illinois.edu, Tel: 1 217 333 0188

Craig K. Abbey: Email:abbey@psych.ucsb.edu, Tel: 1 530 752 1033

Michael F. Insana: Email: mfi@illinois.edu, Tel: 1 217 244 0739

the echo signal-to-noise ratio (eSNR). Basic Fourier optics analysis suggests that we shorten the pulse duration and increase the detector aperture area to concentrate into a small volume as much of the transmitted sound energy as possible. Beam diffraction, sound absorption, and phase aberrations ultimately limit the utility of this straightforward approach, which has prompted investigations into synthetic aperture methods<sup>7,8</sup> and other types of pre- and post- beamformed RF signal filtering.<sup>9-12</sup> Filtering techniques are by necessity adaptive, requiring detailed knowledge of the system's spatiotemporal response and some specific knowledge of tissue statistics and heterogeneity to realize performance enhancements.

We have adopted the ideal-observer strategy of spatially filtering post-beamformed RF echo data in an attempt to improve detection performance for five lesion features closely associated with clinical sonographic breast cancer detection.<sup>1,4</sup> Working in the sampled signal domain, we modeled the RF echo signal as the output of a linear system, and applied stationary Gaussian distributions to model the scattering object and noise.<sup>17</sup> Assuming the isoplanatic response of a linear shift-invariant system, the RF data corresponding to each B-mode image was simulated from one of two classes of correlated multivariate Gaussian distributions. This two-class discrimination task led to an ideal observer decision variable that is quadratic in the echo data and involves the inverse covariance matrix for each class. Large nonstationary covariance matrices were separated into stationary and nonstationary parts and expanded in a power series to facilitate fast computation of their inverses.<sup>1</sup> The linear term in the power series showed that a spatial Wiener filter (SWF) applied to RF data before envelope detection approximated the ideal observer strategy provided the lesions were of low contrast so that the scattering field was approximately wide-sense stationary. We explored the effect of the SWF on task performance comparing the efficiency of human observers viewing images of filtered data with respect to the standard B-mode images. Human observer performance was evaluated through 2AFC psychophysical studies using a panel of five tasks. These tasks isolated features of breast lesions that radiologists typically use to detect breast lesions and discriminate malignant tumors from benign. We found that SWF improves observer performance over conventional B-mode beamforming for four of the five tasks, but surprisingly we found it reduced performance for the one high-contrast lesion task.

In this paper, we more closely examine the effects of the SWF on the clinical tasks, and from the analysis we propose an adaptive method that further improves observer performance. The proposed method addresses deficiencies in the application of the power series expansion to calculate the inverse of the covariance matrices, which in return improved the validity of the linear approximation. The new technique employs an iterative process to compute a filter that adapts to the properties of each RF data set. We call the approach the *iterative spatial Wiener filter* (ISWF). Observer and machine experiments show that the new filter improves performance for all tasks. Image data is now simulated by using the Field II program<sup>21,22</sup> to simulate the impulse response of typical one-dimensional linear arrays, instead of using Gabor pulses; that is a 2-D Gaussian pulses modulated along one axis by the carrier frequency as in our previous studies.<sup>1</sup> The comparison between the results of using the two pulses is also discussed in this paper.

## 2. BACKGROUND AND LITERATURE REVIEW

In this section, we summarize our previous research,<sup>1</sup> where the ideal observer strategy motivated the SWF approach in the RF data domain.

### 2.1 System modeling

A model of image formation is depicted graphically in Fig. 1, in which the variance profile determines whether the lesion has the features of a benign or malignant breast tumor. The object being imaged  $\mathbf{f}$  is arranged from a 2D scattering field into a column vector by *lexicographical* ordering. Then the RF data can be modeled as a noisy linear transformation of the scattering object, given by

$$\mathbf{g} = \mathbf{H}\mathbf{f} + \mathbf{n}, \quad (1)$$

where  $\mathbf{g}$  is the vector of RF frame data and  $\mathbf{H}$  is the system matrix characterizing the transformation. The isoplanatic assumption allows us to represent  $\mathbf{H}$  as a Toeplitz-block Toeplitz matrix.  $\mathbf{n}$  is the object independent system noise, a zero-mean Gaussian random noise process with variance  $\sigma_n^2$ .

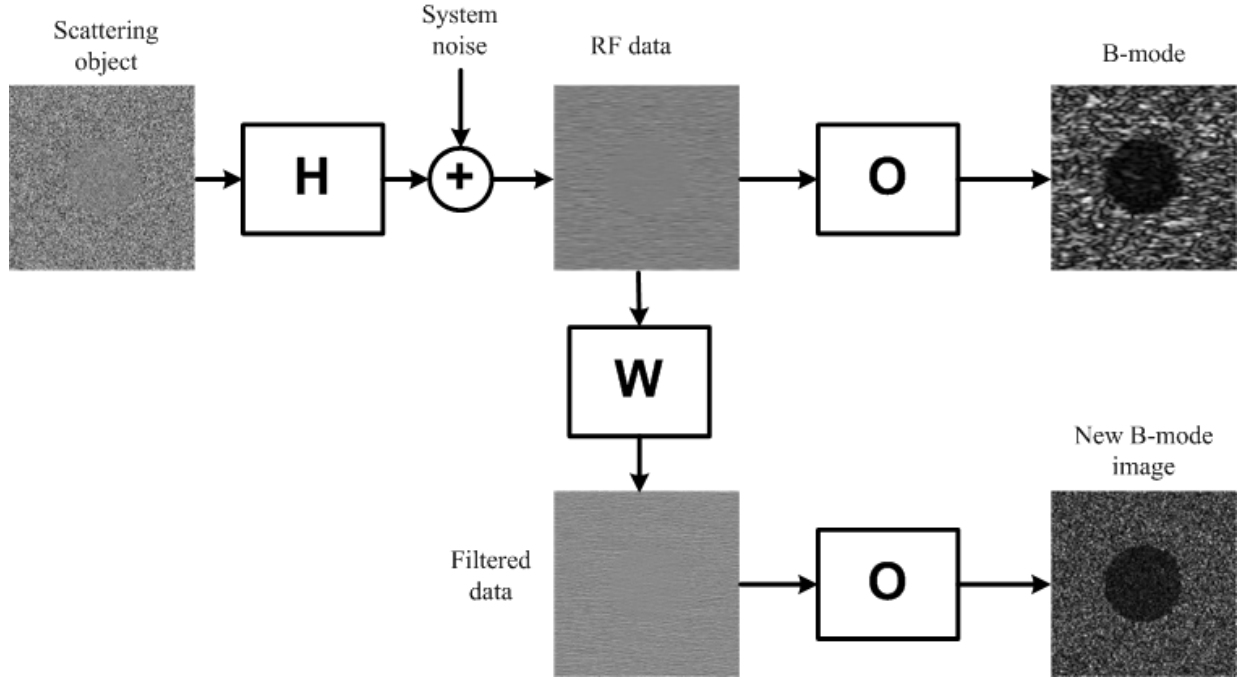


Figure 1. A graphical model of ultrasonic signal processing. The top row shows the formation of a standard B-mode image from a scattering object.  $\mathbf{H}$  represents a linear shift-variant system where each row is a shifted copy of the impulse response function generated using Field II program.<sup>21,22</sup> The bottom row shows the RF data after being SWF filtered and the corresponding B-mode image.

Let  $H_1$  be the hypothesis that  $\mathbf{f}$  represents scattering from a benign lesion and  $H_2$  be the hypothesis that  $\mathbf{f}$  is from a malignant lesion. We model scattering amplitude of tissue under both hypotheses as a zero-mean, multivariate normal (MVN) process, with a common scattering variance,  $\sigma_{\text{obj}}^2$ , that characterizes the overall intensity. The difference between the two hypotheses is encoded in diagonal deviation matrices  $\mathbf{S}_1$  and  $\mathbf{S}_2$ . Thus the distributions of  $\mathbf{f}$  under each hypothesis are given by

$$\begin{aligned} H_1 : \mathbf{f} &\sim \text{MVN}(\mathbf{0}, \sigma_{\text{obj}}^2(\mathbf{I} + \mathbf{S}_1)) \\ H_2 : \mathbf{f} &\sim \text{MVN}(\mathbf{0}, \sigma_{\text{obj}}^2(\mathbf{I} + \mathbf{S}_2)) \end{aligned} \quad (2)$$

The elements of diagonal matrix  $\mathbf{S}_1$  and  $\mathbf{S}_2$  can be positive or negative, but they must be greater than -1 to ensure positive variance. In Fig. 2 we display five modeled features for  $\mathbf{S}_1$  and  $\mathbf{S}_2$ , corresponding to five typical tasks involved with cancer detection.

Combining equations (1) and (2), we find the RF data for the two hypotheses are also multivariate normal:

$$\begin{aligned} H_1 : \mathbf{g} &\sim \text{MVN}(\mathbf{0}, \Sigma_1) \\ H_2 : \mathbf{g} &\sim \text{MVN}(\mathbf{0}, \Sigma_2) \end{aligned} \quad (3)$$

where

$$\Sigma_i = \sigma_{\text{obj}}^2 \mathbf{H}(\mathbf{I} + \mathbf{S}_i) \mathbf{H}^t + \sigma_n^2 \mathbf{I} \quad (4)$$

All information about the scattering object and system is contained in the covariance matrices  $\Sigma_i$ . B-mode data are scan converted to produce B-mode images using the non-linear operator  $\mathbf{O}$ , such that  $\mathbf{b} = \mathbf{O}\mathbf{g}$ .

## 2.2 Ideal Observer

The test statistic for binary hypothesis testing is given by the ratio of the probability density function for RF data in  $H_2$  to that in  $H_1$ .<sup>23</sup> By taking the logarithm of this ratio and ignoring terms unrelated to the data, we obtained the decision variable for the ideal observer, given by

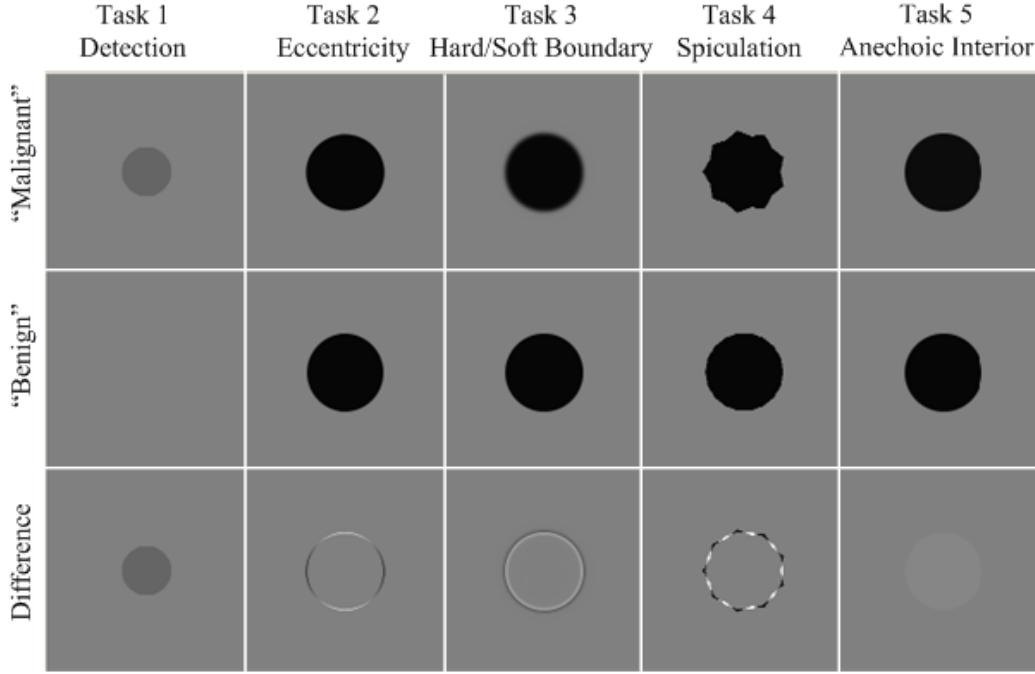


Figure 2. Variance profiles of “Malignant” and “Benign” scattering objects of the five tasks. The third row is the difference in variance profiles. The five tasks represent: detection of a hypoechoic lesion (Task 1), discrimination of an elongated eccentric lesion from a circular lesion (Task 2), discrimination of a soft, poorly defined boundary from a well-circumscribed lesion (Task 3), discrimination boundary irregularities from a smooth boundary (Task 4), and discrimination hypoechoic from anechoic lesion interiors (Task 5)<sup>1</sup>

$$\lambda(\mathbf{g}) = \ln \frac{p(\mathbf{g}|\mathbf{H}_2)}{p(\mathbf{g}|\mathbf{H}_1)} \cong \frac{1}{2} \mathbf{g}^t (\boldsymbol{\Sigma}_1^{-1} - \boldsymbol{\Sigma}_2^{-1}) \mathbf{g}. \quad (5)$$

There is a computational challenge in calculating the ideal observer (5), because  $\boldsymbol{\Sigma}_i$  are too large to be inverted accurately using straightforward computing methods. In next step, we will explore the technique for inverting these large non-stationary covariance matrices.

### 2.3 The spatial Wiener filter

Assuming  $\mathbf{H}$  is a circulant matrix, we can separate the covariance matrices into stationary and non-stationary components,

$$\begin{aligned} \boldsymbol{\Sigma}_i &= \sigma_{\text{obj}}^2 \mathbf{H} \mathbf{H}^t + \sigma_n^2 \mathbf{I} + \sigma_{\text{obj}}^2 \mathbf{H} \mathbf{S}_i \mathbf{H}^t \\ &= \boldsymbol{\Sigma}_0 + \Delta \boldsymbol{\Sigma}_i, \end{aligned} \quad (6)$$

where  $\boldsymbol{\Sigma}_0$  is the stationary part, whose inverse can be efficiently calculated by a Fourier technique,<sup>23</sup> and  $\Delta \boldsymbol{\Sigma}_i$  is the non-stationary part that depends on variance profile  $\mathbf{S}_i$ .

Expanding  $\boldsymbol{\Sigma}_i^{-1}$  in a power series and truncating after the first order term, we obtain the linear approximation of the ideal-observer test statistic,

$$\lambda(\mathbf{g}) \approx \frac{\sigma_{\text{obj}}^2}{2} \mathbf{g}^t \boldsymbol{\Sigma}_0^{-1} \mathbf{H} (\mathbf{S}_2 - \mathbf{S}_1) \mathbf{H}^t \boldsymbol{\Sigma}_0^{-1} \mathbf{g}. \quad (7)$$

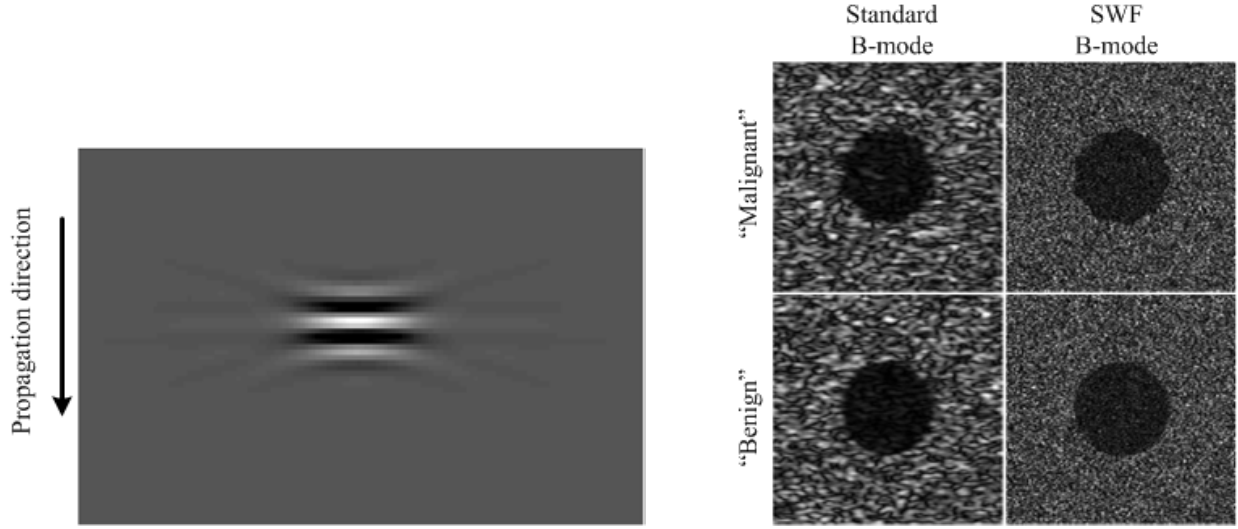


Figure 3. (left) Pulse-echo psf of a system generated by the Field II program. (right) Examples of standard and spatial Wiener filtered B-mode images from the same RF data for task 4

The factors  $\mathbf{H}^t \Sigma_0^{-1} \mathbf{g}$  are recognized as the spatial Wiener filtered version of RF data. It suggests that applying the SWF to the RF data before envelope detection recovers some diagnostic information that would otherwise be lost. Thus spatial Wiener filtering in the RF domain may improve the efficiency for visual discrimination tasks.

### 3. IMPLEMENTATION AND DISCUSSION ON THE SWF

#### 3.1 Methods

The Fig. 3 (left) shows the 2-D pulse-echo point spread function (psf) of the system at focus generated by the Field II program.<sup>21,22</sup> Parameters were set to model the Siemens Antares system response at a 40-mm transmit/receive focal length with a VF10-5 1-D linear array transducer. We use 7.2 MHz carrier frequency sampled at 40 MHz, which results in an axial sampling interval  $\Delta x = 0.02\text{mm}$  and a lateral sampling interval  $\Delta y = 0.1\text{mm}$ . Element pitch was set to 0.198 mm with 5% kerf, and the transmit and receive apertures were 10 mm  $\times$  20 mm (96 elements). The bandwidth was set to 51% of the carrier frequency, and the echo SNR of the system was 45.5 dB. From shift invariant pulse-echo impulse response, we constructed a circulant system matrix  $\mathbf{H}$  used to both model the RF data and develop the SWF.

By assessing the five clinical tasks in Fig. 2, we quantify how much information is lost when converting from RF data to envelope images, and how much information can be recovered by applying the SWF to the RF data before computing the envelope. The five clinical tasks were based on candidate features that trained experts are likely to look for in the process of discriminating malignant from benign breast lesions with ultrasound. The scattering object used in simulation is defined by its variance profile, which is classified as either “malignant” or “benign” as shown in Fig. 2. Examples of standard and SWF B-mode images for task 4 are shown in Fig. 3 (right). In each task, the controlled parameter determining the difficulty of the task is the difference between the variance maps under the two hypothesis. To place all tasks on a common scale, we define an object contrast factor as the integrated absolute value of the difference between the malignant variance profile and the benign one normalized by the object variance, given as

$$C = \sum_i |[\mathbf{S}_1 - \mathbf{S}_2]_{ii}| \Delta x \Delta y. \quad (8)$$

The information loss when converting from the RF data to the envelope image is evaluated through the *observer efficiency* which is calculated by combining the ideal observer on the RF data in (5) and the Smith-Wagner observer, acting as the ideal observer on envelope images, given by

$$\lambda_{\text{SW}}(\mathbf{b}) = \mathbf{b}^t (\mathbf{S}_2 - \mathbf{S}_1) \mathbf{b}. \quad (9)$$

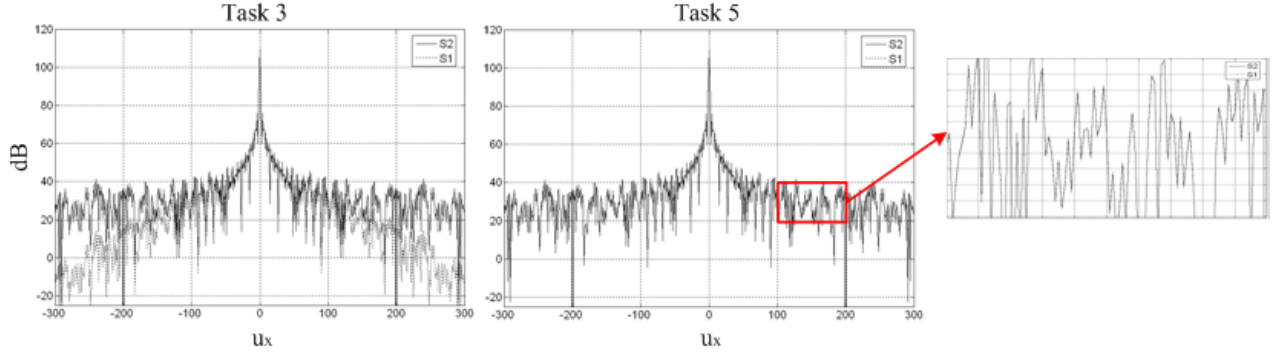


Figure 4. The Fourier transform of  $\mathbf{S}_i$  versus spatial frequency  $u_x$  for task 3 and task 5. At high spatial frequencies, the frequency spectra of for the two tasks are separated in task 3 (left) while the magnified view shows that they are on top of each other in task 5 (right).

The ideal observer test statistic,  $\lambda(\mathbf{g})$ , is calculated by using the iterative implementation of the power series.<sup>1</sup> However, unlike our previous research that uses the Gabor pulse as the psf of the system, the psf generated by Field II has fine structure that extends significantly outside the main lobe of the beam. Consequently when calculating the inverse of the non-stationary covariance matrix, up to 50 terms of the power series are required for the Field II generated psf to reach convergence instead of 10 terms as in the previous research for the Gabor pulse generated psf.

For the ideal observer and Smith-Wagner observer, 2000 pairs of images were generated for each task. If we let  $\mathbf{g}_{1,i}$  be the RF frame from  $H_1$  in the  $i$ th trial and  $\mathbf{g}_{2,i}$  be the RF frame from  $H_2$ , then the trial score,  $o_i$ , is given by

$$o_i = \text{step}(\lambda(\mathbf{g}_{2,i}) - \lambda(\mathbf{g}_{1,i})) \quad (10)$$

where the step function is equal to 1 for positive argument and 0 for negative. The proportion correct,  $P_C$ , is defined as the expectation of the trial score. Under general assumptions,  $P_C$  is monotonically related to the detectability index as<sup>23</sup>

$$d_A = 2\text{erf}^{-1}(2P_C - 1), \quad (11)$$

in which  $\text{erf}^{-1}$  is the inverse error function. If we define  $C_{\text{env}}$  as the object contrast factor for Smith-Wagner observer viewing the envelope data, and  $C_{\text{RF}}$  as the contrast parameter setting that produces the equivalent performance in the ideal observer viewing the RF data ( $d_{A-SW} = d_{A-Ideal}$ ), then the observer efficiency, or the information loss, when converting from the RF data to the envelope images is approximated by,

$$\eta = 100\% \times \frac{C_{\text{RF}}}{C_{\text{env}}}. \quad (12)$$

Human-observer performance was assessed through 2AFC psychophysical studies. A total of 4 observers participated in the experiments. The experiments have been carried out at the Vision and Image Understanding Lab, University of California, Santa-Barbara. Pilot studies on independent sets of images were used to find object contrast factors such that human observer performance in the standard B-mode images would be approximately 80% correct. This performance level leaves reasonable range for investigating the improvement due to signal processing.<sup>24</sup> In each task, the standard B-mode images and the various post-processing envelope images were generated from the same RF data.

### 3.2 Discussion of SWF

In previous studies,<sup>1</sup> we found that application of the SWF improves the visual detection performance for the first four tasks, but reduces detection performance in task 5. We begin our discussion by investigating what is different in the five visual tasks. The third row of the Fig. 2 shows differences between “Malignant” and “Benign” variance profiles of the five tasks. The difference in tasks 2-4 is primarily in edges of the lesions and thus at high spatial frequency, while that in task 1 and task 5 is in the contrast inside the lesions. However, in

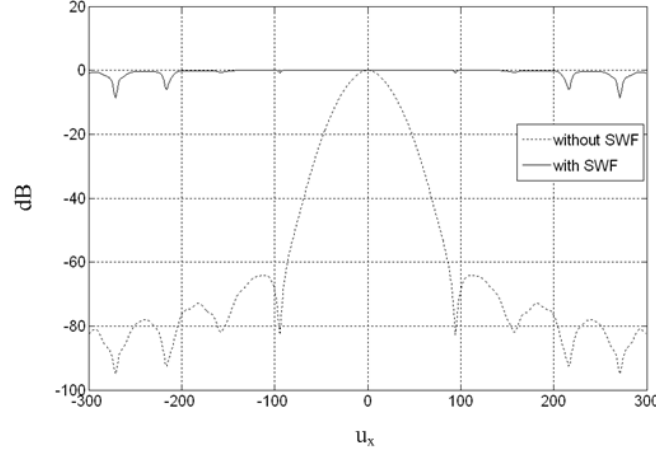


Figure 5. The normalized power spectra of the ultrasonic pulse with and without SWF

task 1 the wide-sense stationary approximation holds for the low-contrast lesions of each individual image much better than it does for the high-contrast lesions of task 5. Therefore the linear approximation is nearly ideal and we do not expect any processing to significantly improve observer performance for task 1.

Let's consider the edgy tasks 2-4, where human observer efficiency for standard B-mode imaging is known to be very low.<sup>1</sup> Fig. 4 (left) shows that the difference in the frequency spectra for the lesion of task 3 under the two hypotheses is clearly at high spatial frequencies. However, there is almost no difference in those spectra for the high-contrast/very high-contrast detection of task 5 (Fig. 4, right). Furthermore, Fig. 5 show that the SWF acts to spectrally 'whiten' the system response function, which it can do for our relatively high eSNR conditions. SWF enhances high frequencies by decorrelating the RF signals. Decorrelation is not new topic, but we now have a first-principles reason for applying it! We may also think of the SWF as suppressing low frequencies in favor of high frequencies. Put yet another way, the SWF improves performance for edgy tasks by providing the decision maker with more statistically independent image samples. Since the information in tasks 2-4 is concentrated near the boundary region, adding independent samples influences performance significantly.

Why does the high-contrast nature of each lesion in task 2-4 not also negate the stationary assumption as it did in task 5? The answer appears to be that the ideal observer is seeking a signal known exactly (SKE), and therefore ignores the filtering errors at the lesion interior for task 2-4. The SKE nature of the human experiments allows them to do the same. In task 5, all the information is at the center of the lesion, so that region cannot be ignored when deciding. The SWF, which is designed to filter the background region, will naturally fail to improve performance in task 5. Thus we find our motivation for developing an adaptive spatial filter that improves the performance of the linear approximation to the ideal strategy. The alternative is to add more terms to the power series expansion of the covariance matrices which does not advise a clear method for generating images.

#### 4. ITERATIVE SPATIAL WIENER FILTER

##### 4.1 The adaptive filter

The linear approximation to the power series of  $(\mathbf{I} - \mathbf{A})^{-1} \approx \mathbf{I} + \mathbf{A}$  is a good approximation iff all eigenvalues of  $\mathbf{A}$  are much smaller than 1. This condition is reasonably well met for tasks 1-4 but not 5. Instead of separating the covariance matrix into stationary and non-stationary components, we combine them into average and difference matrices. Denoting  $\mathbf{S}_a = 0.5(\mathbf{S}_1 + \mathbf{S}_2)$  and  $\Delta\mathbf{S}_a = 0.5(\mathbf{S}_2 - \mathbf{S}_1)$ , the associated covariance matrices become  $\Sigma_1 = \Sigma_a - \Delta\Sigma$  and  $\Sigma_2 = \Sigma_a + \Delta\Sigma$ , with

$$\Sigma_a = \sigma_{\text{obj}}^2 \mathbf{H}(\mathbf{I} + \mathbf{S}_a)\mathbf{H}^t + \sigma_n^2 \mathbf{I} \text{ and } \Delta\Sigma = \sigma_{\text{obj}}^2 \mathbf{H}\mathbf{S}_a\mathbf{H}^t. \quad (13)$$

In this way,  $\pm\Delta\mathbf{S}_a$  plays the role of  $\mathbf{S}_i$  in SWF, and both are almost equal to zero since  $\mathbf{S}_1 \approx \mathbf{S}_2$ . Consequently the accuracy of the linear approximation is improved.

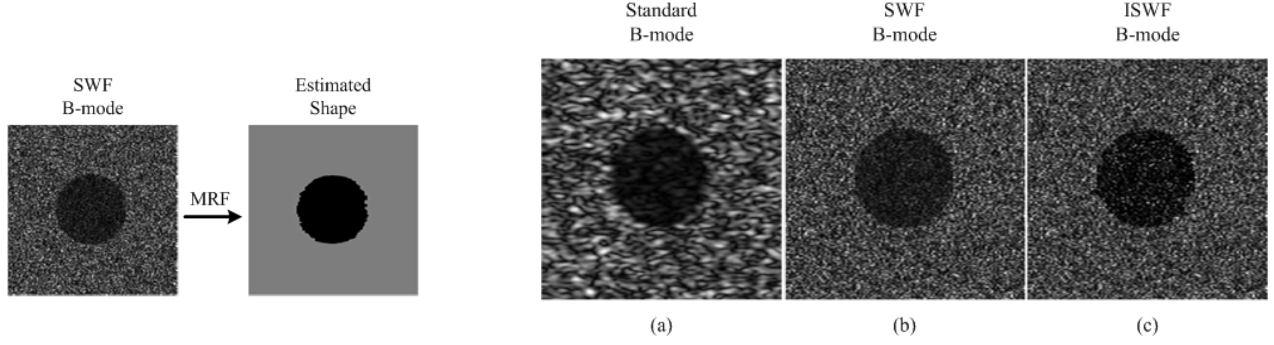


Figure 6. (left) Segmentation of the SWF envelope image for the benign lesion in task 5. (right) Example images of benign lesions from task 5.

The ideal-observer test statistic now becomes,

$$\lambda(\mathbf{g}) \approx \frac{\sigma_{\text{obj}}^2}{2} \mathbf{g}^t \boldsymbol{\Sigma}_a^{-1} \mathbf{H}(\mathbf{S}_2 - \mathbf{S}_1) \mathbf{H}^t \boldsymbol{\Sigma}_a^{-1} \mathbf{g} \quad (14)$$

This formula assumes that we can invert the matrix  $\boldsymbol{\Sigma}_a$ . However,  $\boldsymbol{\Sigma}_a$  is a non-stationary and hence Fourier methods do not apply. Instead, we apply the power series approach to calculate this inverse, using a stationary/nonstationary decomposition,  $\boldsymbol{\Sigma}_a = \sigma_{\text{obj}}^2 \mathbf{H}(\mathbf{I} + \mathbf{S}_a) \mathbf{H}^t + \sigma_n^2 \mathbf{I}$ . This yields an iterative formula to compute  $\sigma_{\text{obj}}^2 \mathbf{H}^t \boldsymbol{\Sigma}_a^{-1} \mathbf{g}$ . We call it the *Iterative Spatial Wiener filter* (ISWF).

The iterative scheme is initialized by  $\mathbf{q}_0 = \mathbf{p}_0 = \sigma_{\text{obj}}^2 \mathbf{H}^t \boldsymbol{\Sigma}_0^{-1} \mathbf{g}$ . Then the process is given by

$$\mathbf{q}_{i+1} = \sigma_{\text{obj}}^2 \mathbf{H}^t \boldsymbol{\Sigma}_0^{-1} \mathbf{H} \mathbf{S}_a \mathbf{q}_i \text{ and } \mathbf{p}_{i+1} = \mathbf{p}_i + \mathbf{q}_{i+1}. \quad (15)$$

From (15), we see that ISWF adapts to include statistical properties of the RF data throughout the field. The lesion is specified by the parameter  $\mathbf{S}_a$ . So this process requires that we first calculate  $\mathbf{S}_a$  before taking iterations. From the definition of  $\mathbf{S}_a$ , we can calculate it through  $\mathbf{S}_1$  and  $\mathbf{S}_2$ , where  $\mathbf{S}_1$  and  $\mathbf{S}_2$  are estimated from RF data using segmentation.

## 4.2 Segmentation

We have proposed a segmentation algorithm which makes use of a Markov random field (MRF) model.<sup>25,26</sup> In this model, image pixel values in one segmented region are assigned to a Gaussian distribution with specific parameters (mean and variance) for each class. Then iterations are taken until the segmentation becomes stable. The parameters are updated after each iteration. The core of this method is the adaptive clustering algorithm of Papas,<sup>27</sup> which has been applied for B-mode images by Ashton *et al.*<sup>28</sup> In their research, they decompose the B-mode image into multiple layers (Wavelet Decomposition), so that the Gaussian distribution can be applied for the lowest resolution images. Segmentation is applied for each layer from the lowest to the highest resolutions. This process is computationally intensive. In our application, we also have the RF data and the system impulse response function. Using these, we can implement the SWF and obtain the SWF envelope image. The edges of the lesion on the SWF envelope are more delineated than on the standard B-mode images, and the distribution of pixel's values can be assumed Gaussian with an error is acceptable for our purpose. Therefore, we can modify the algorithm to perform segmentation on the envelope of SWF data. By doing so, we don't need to decompose the images into multi-resolution levels, thus reducing computation time. Fig. 6 (left) shows an example of the estimated shape of the variance profile obtained from segmentation of the SWF B-mode image.

We also realize that the SWF plays a role as an inverse filter, restoring the original image blurred by the psf of the system, so the SWF data may be considered as a coarse estimate of the scattering object. Combining with (2), we can estimate  $\sigma_{\text{obj}}^2$  from the mean square pixel value of the background region. The value for  $\mathbf{S}_i$  inside the lesion may be estimated by measuring the mean-square image value inside the lesion and dividing it by the estimated  $\hat{\sigma}_{\text{obj}}^2$ . However, we modify the process slightly by just dividing the squared magnitude of

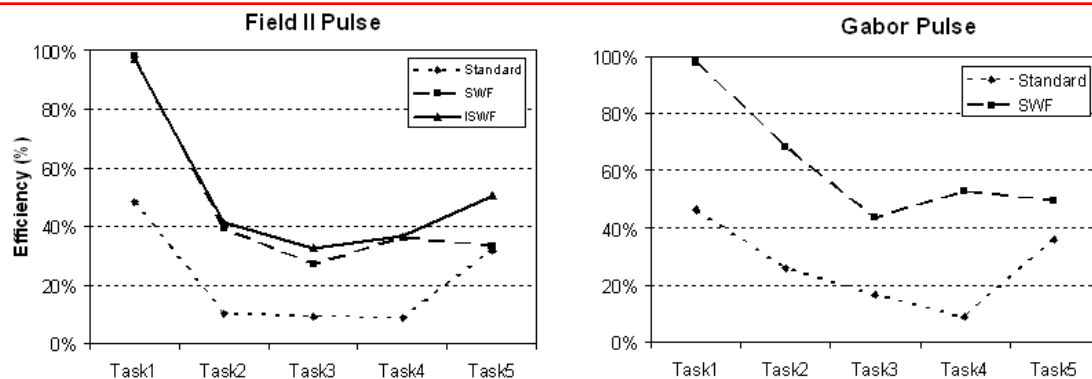


Figure 7. Approximate efficiencies of the envelope observer for the five tasks defined in Fig 2. Results obtained using the psf generated by the Field II simulation program<sup>21,22</sup> (left) and using Gabor pulses (sinusoid with a Gaussian-modulated amplitude) as taken from the previous work<sup>1</sup> (right).

each pixel inside the lesion by  $\hat{\sigma}_{\text{obj}}^2$  to take advantages of the inherent contrast amplification with each iteration. Segmentation using the MRF model works well for most of the lesions in our five typical tasks. We only have a problem in task 3, where malignant lesions have smooth boundaries. The two-level assumption for the MRF model conflicts with the smooth boundary and creates unavoidable segmentation errors.

Applying the segmented variance profile to the iterative process, we calculated the ISWF B-mode images, as shown in Fig. 6(c). To compare with the SWF B-mode image (b), the ISWF has adapted to the data despite the segmentation errors. Furthermore, it amplifies the low contrast scattering signal inside the lesion that can enhance the performance for task 5.

## 5. RESULTS

### 5.1 Predicted Observer Efficiency

The approximate efficiencies of the envelope observer (ratio of detectability index for the Smith-Wagner (SW) observer to that of the ideal observer) are shown in Fig. 7 for the five visual tasks. The SW observer was developed based on analysis of the B-mode data more than 25 years ago specifically for detection as in task 1.<sup>18,19</sup> Since the greatest loss of performance occurs during the conversion from RF to B-mode data, we found that the efficiency of the envelope observer is reasonably predictive of trained human responses for these tasks.<sup>1</sup> Fig. 7 summarizes the efficiencies using standard B-mode images and those filtered using SWF and ISWF methods. On the left, images were generated using the Field II program to simulate properties of the Siemens Antares system, and on the right, images were generated using a Gabor pulse with similar images system properties. These data are taken from the previous work<sup>1</sup> with a correction to the equation for calculating the efficiency [1, Eq(17)] to remove the square operation from the ratio of contrasts. Detectability indices are computed using the mean test statistic value from 2000 independent pairs of image data. The ideal observer test statistic for data generated with Fields II pulses was calculated using 50 terms in the covariance power series to reach convergence for all tasks; only 10 terms were needed for the Gabor pulse.

Comparing the standard B-mode and SWF results from the left and right charts, we see there is a loss of efficiency for the Field II pulse results compared with the Gabor pulse results, except for task 1 where efficiencies are comparable as expected. Unlike Gabor pulses, Field II pulses have a fine structure of wave energy that extends spatially a distance several times the main lobe dimension. This structure is not computation error; rather it reflects the incomplete cancellation of edge waves known to emerge from transducer array elements. The ISWF efficiencies are equivalent to the SWF results for tasks 1-4, however ISWF improved efficiencies relative to the SWF from 33% to 50% for task 5. The lowest performance using ISWF images was obtained in task 3, for which the segmentation algorithm generated the largest errors because of the soft lesion boundaries.

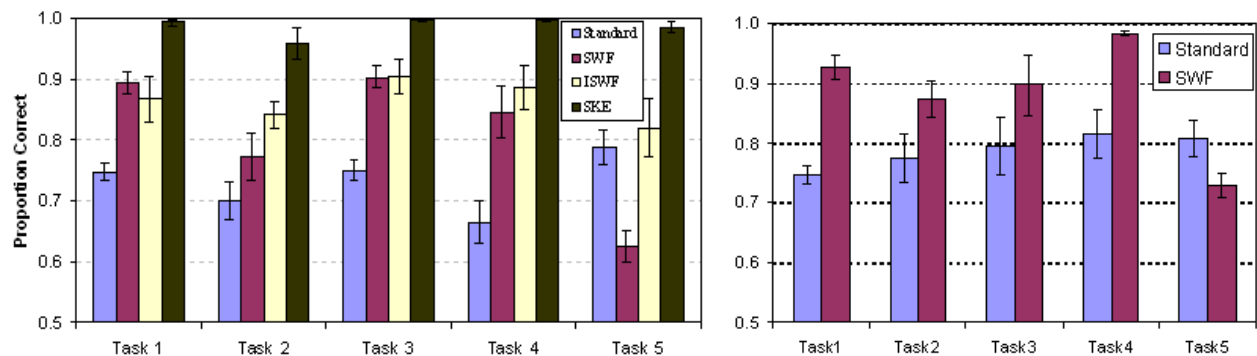


Figure 8. Human observer performance as measured as proportion of correct responses from 2AFC trials. Results obtained using the psf generated by the Field II simulation program<sup>21, 22</sup> (left) and using Gabor pulses as taken from the previous work<sup>1</sup> (right). Results on the left labeled SKE are from ISWF images in which the geometry of the lesion is known exactly.

## 5.2 Measured human observer performance

Fig. 8 charts the performance of human observers as measured in 2AFC psychophysical studies for the same class of data described in Fig. 2 and Fig. 7. The results are an average of responses from four trained observers viewing 400 image pairs in each of the five tasks. A pilot study was conducted for determine how to adjust the contrast so that the average performance viewing B-mode images was approximately 80%.

We cannot determine from these data whether human performance was affected when observers viewed images formed using the more realistic Field II pulses compared with that of the Gabor pulses because contrasts were adjusted independently to approximate 80% correct responses for each task. The fact that the proportions correct for standard B-mode images in tasks 2-4 were below the targeted 80% value is noteworthy. In the pilot studies, where contrast was set, we involved two very experienced observers. Including results from two less experienced observers lowered the average, suggesting that further training may be required for the edgy tasks 2-4, which show lowest efficiency.

Human performance involving SWF and ISWF images was statistically equivalent in tasks 1-4. Only in task 5 was performance substantially improved from  $63\pm 2\%$  to  $82\pm 4\%$  correct. Further, we see that if the shape of the lesion is known exactly when forming the iterative spatial Wiener filter (see the ISWF results labeled SKE in Fig. 8, left), the visual task is simplified so much that the proportion correct is nearly 100%. This mainly tells us that segmentation errors are limiting performance of the ISWF approach.

The price paid for use of ISWF is computation time. Standard B-mode images are generated at speeds far in excess of video rates, depending on the field of view and ultimately the speed of sound in the body. The filtering applied in SWF images requires significant computation time (many second on a PC), although the exact time depends on the processor. It is conceivable that rates approaching 30 fps are possible for SWF images. However, the iterations intrinsic to the filtering in ISWF images require significant more processing time (many minutes on a PC), making it unlikely to achieve real-time frame rates. Fast processing of ideal observer strategies is a topic of current interest. To determine if investment in such approaches is worthwhile, we would need to conduct a clinical trial to evaluate the cost/benefit ratio.

## 6. SUMMARY AND CONCLUSIONS

The ideal observer formalism reveals optimal strategies for imaging specific features deemed critical for breast imaging diagnosis. The challenge is to first interpret medical diagnostic problems in terms of likelihood functions as required for the analysis, and then to devise fast techniques that implement the ideal strategy or its approximation. During our investigations, we find that the signal processing techniques emerge that were proposed over the past few decades, especially beamforming methods like spatial filtering, deconvolution, and minimum-variance techniques. The ideal observer formalism is a first-principles approach for designing beamformers (detector stage of the ultrasonic system) that are ideal for specific clinical tasks.

Spectral analysis of the five visual tasks associated with breast lesion classification and the spatial Wiener filter provided further insights into the performance of SWF images relative to standard B-mode images. This analysis suggested an iterative (ISFW) approach that we found significantly improved observer performance for task 5, which requires observers to discriminate between lesions with two very low echogenicity levels. To implement the ISWF method, we need to first segment the suspected lesion areas in order to design the adaptive filter. Observer data viewing ISWF images suggest that the performance is primarily limited by segmentation errors.

We conclude that approximations to the ideal observer strategy are capable of improving visual detection of five individual features associated with breast cancer diagnosis as identified by an experience radiologist. We do not yet know how performance is affected by combining these tasks. The utility of the approach depends on the cost/benefit ratio that has yet to be determined

## ACKNOWLEDGMENTS

This work is supported by NIH under award No. CA118294.

## REFERENCES

- [1] C.K. Abbey, R.J. Zemp, J. Liu, K.K. Lindfors, M.F. Insana, "Observer efficiency in discrimination tasks simulating malignant and benign breast lesions imaged with ultrasound," *IEEE Trans Med Imaging*, (25):pp. 198-209, 2006.
- [2] C.K. Abbey, R.J. Zemp, M.F. Insana, "Pre-envelope deconvolution for increased lesion detection in ultrasonic imaging," *Proc. SPIE*, (5034):pp. 280-288, 2003.
- [3] C.K. Abbey, R.J. Zemp, J. Liu, K.K. Lindfors, M.F. Insana, "Observer efficiency in boundary discrimination tasks related to assessment of breast lesions with ultrasound," *Proc. SPIE Med. Imag. (Y. Jiang and M. P. Eckstein Ed.s)*, (6146), 2006.
- [4] C.K. Abbey, N.Q. Nguyen, M.F. Insana, "An ideal observer approach to beamforming," *Proc. SPIE*, (6146):pp. 1-8, 2008.
- [5] S.S. Brunke, M.F. Insana, J.J. Dahl, C. Hansen, M. Ashfaq, H. Ermert, "An ultrasound research interface for a clinical system," *IEEE Trans UFFC*, (54):pp. 198-210, 2007.
- [6] J.C. Bamber., "Speckle reduction," *Clin Diagn Ultrasound*, (28):pp. 55-67, 1993.
- [7] M. Karaman, P-C. Li, M. O'Donnell, "Synthetic aperture imaging for small scale systems," *IEEE Trans. Ultrason. Ferroelectr. Freq. Control*, (42):pp. 429-42, 1995.
- [8] G.E. Trahey, L. F. Nock, "Synthetic receive aperture imaging with phase correction for motion and for tissue inhomogeneities. Part I: Basic principles," *IEEE Trans. Ultrason. Ferroelectr. Freq. Control*, (39):pp. 489-95, 1992
- [9] O. Michailovich, D. Adam, "A novel approach to the 2-D blind deconvolution problem in medical ultrasound," *IEEE Trans Med Imaging*, (24):pp. 86-104, 2005.
- [10] K.S. Kim, J. Liu, M.F. Insana, "Efficiency array beamforming by spatial filtering for ultrasound B-mode imaging," *J Acoust Soc Am*, (120):pp. 852-61, 2006.
- [11] J.F. Synnevag, A. Austeng, S. Holm, "Adaptive beamforming applied to medical ultrasound imaging," *IEEE Trans. Ultrason. Ferroelectr. Freq. Control*, (54):pp. 1606-13, 2007
- [12] J.A. Jensen, "Deconvolution of ultrasound images," *Ultrasonic Imaging*, (14):pp. 1-15, 1992.
- [13] M. Fatemi, A.C. Kak, "Ultrasonic B-scan imaging: theory for image formation and a technique for image restoration," *Ultrasonic Imaging*, (2):pp. 1-47, 1980.
- [14] H.H. Barrett, "Objective assessment of image quality: effects of quantum noise and object variability," *J Opt Soc Am A*, (7):pp. 1266-78, 1990.
- [15] American College of Radiology, *Breast Imaging Reporting and Data System Atlas*, Reston, VA, 2003.
- [16] R.F. Wagner and H.H. Barrett, "Quadratic tasks and the ideal observer," *Proc. SPIE*, (767):pp. 306-309, 1987.
- [17] R.J. Zemp, C.K. Abbey, M.F. Insana, "Linear System model for ultrasonic imaging: Application to Signal Statistics," *IEEE Trans UFFC*, (6):pp. 642-654, 2003.

- [18] R.F. Wagner, S.W. Smith, J.M. Sandrik, H. Lopez, "Statistics of speckle in ultrasound B-scans," *IEEE Trans. Sonics Ultrason.*,(30),pp. 156-163, 1983.
- [19] S.W. Smith, R.F. Wagner, J.M. Sandrik, H. Lopez, "Low-contrast detectability and contrast/detail analysis in medical ultrasound," *IEEE Trans. Sonics Ultrason.*,(30):pp. 164-173, 1983.
- [20] G.H. Golub and C.F. Van Loan, *Matrix Computations*, Johns Hopkins, third edition, 1996.
- [21] J.A. Jensen and N. B. Svendsen, "Calculation of pressure fields from arbitrarily shaped, apodized, and excited ultrasound transducers," *IEEE Trans. Ultrason. Ferroelec. Freq. Contr.* (39):pp. 262-267, 1992.
- [22] J. A. Jensen, "Field: A program for simulating ultrasound systems". *Med. Biol. Eng. Comp.*, 10th Nordic-Baltic Conference on Biomedical Imaging, (4), Supplement 1, Part 1:pp. 351-353, 1996.
- [23] H.H. Barrett, K.J. Myers, *Foundations of Image Science*, John Wiley & Sons, Hoboken, New Jersey, 2004.
- [24] D.M. Green and J.A. Swets, *Signal Detection Theory and Psychophysics*, Wiley, NY, 1966.
- [25] B.J. Besag, "On the statistical analysis of dirty pictures," *J. Royal Statist. Soc. B.* (3):pp. 259-302, 1986.
- [26] J.S. Geman and D. Geman, "Stochastic Relaxation, Gibbs Distribution and the Bayesian Restoration of Images," *IEEE Trans. Pattern Anal. Mach. Intel.*, (6):pp. 721-741, 1984.
- [27] T.N. Pappas, "An adaptive clustering algorithm for image segmentation," *IEEE Trans. Signal Process.*, (4):pp. 901-914, 1992.
- [28] E.A. Ashton, K.J. Parker, "Multiple resolution Bayesian segmentation of ultrasound images," *Ultrasonic Imaging*, (2):pp. 291-304, 1995.
- [29] M.P. Eckstein, A.J. Ahumanda, A.B. Watson, "Visual signal detection in structured backgrounds, II. Effect of contrast gain control, background variations and white noise," *J Opt Soc Am.* (14):pp. 2406-2419, 1997.
- [30] A.E. Burgess, B. Colborne, "Visual signal detection. IV. Observer inconsistency," *J Opt Soc Am.* (4):pp. 617-627, 1988.
- [31] A.E. Burgess, H. Ghandeharian, "Visual signal detection. II. Signal location identification," *J Opt Soc Am.* (8):pp. 906-910, 1984.
- [32] D.G. Pelli, "Uncertainty explains many aspects of visual contrast detection and discrimination," *J Opt Soc Am.* (9):pp. 1508-1532, 1985.